# The 3 November Tornadic Event during Sydney 2000: Storm Evolution and the Role of Low-Level Boundaries

DAVID M. L. SILLS,* JAMES W. WILSON,+ PAUL I. JOE,* DONALD W. BURGESS,# ROBERT M. WEBB,@ AND NEIL I. FOX&,**

*Cloud Physics Research Division, Meteorological Service of Canada, King City, Ontario, Canada
+National Center for Atmospheric Research, Boulder, Colorado
#NOAA/National Severe Storms Laboratory, Norman, Oklahoma
@Bureau of Meteorology, Sydney, New South Wales, Australia
&University of Salford, Greater Manchester, United Kingdom

(Manuscript received 20 June 2002, in final form 4 March 2003)

ABSTRACT

Several severe thunderstorms, including a tornadic supercell, developed on the afternoon of 3 November 2000, during the Sydney 2000 Forecast Demonstration Project. Severe weather included three tornadoes, damaging wind gusts, hail to 7-cm diameter, and heavy rain causing flash flooding. A unique dataset was collected including data from two Doppler radars, a surface mesonet, enhanced upper-air profiling, storm photography, and a storm damage survey. Synoptic-scale forcing was weak and mesoscale factors were central to the development of severe weather. In particular, low-level boundaries such as gust fronts and the sea-breeze front played critical roles in the initiation and enhancement of storms, the motion of storms, and the generation of rotation at low levels. The complex and often subtle boundary interactions that led to the development of the tornadic supercell in this case highlight the need for advanced detection and prediction tools to improve the warning capacity for such events.

## 1. Introduction

The Sydney 2000 Forecast Demonstration Project (FDP) was undertaken to demonstrate both the capabilities of modern nowcasting systems and the benefits associated with their application in real time (Keenan et al. 2002). Meteorological instrumentation used to support this project was located in the Sydney region of eastern New South Wales (NSW), Australia, and consisted of three radars, a mesonet, and upper-air profiling systems. The project ran from 5 September 2000 to 16 November 2000 and included nowcasting support during the Sydney Summer Olympic Games.

Severe thunderstorms[1] developed on the afternoon of 3 November 2000 and moved through the project area within close range of two Doppler radars. The strongest of these storms—an intense supercell—produced three weak tornadoes, damaging wind gusts, giant hail, and heavy rain in the western suburbs of Sydney resulting in damage to about 300 properties. Numerous boundary layer convergence lines were detected (hereafter referred to as boundaries), including gust fronts and the sea-breeze front, and their interactions played a critical role in the development of severe weather on this day. Thus, the event yielded a unique dataset for the investigation of tornadic supercell evolution and boundary interactions in a region (indeed a hemisphere) that is not currently well represented in the related refereed literature.

Section 2 discusses previous research relevant to this study. Section 3 provides the sources of data and the methodology used for this investigation. Section 4 describes the prestorm synoptic and mesoscale environments. Section 5 examines in detail the severe storms and their evolution. Section 6 discusses the different ways in which boundaries contributed to this event and provides suggestions for improved operational nowcasting of such events. The study's conclusions are presented in section 7. The performance of FDP severe weather algorithms on this day is examined by Joe et al. (2004, in this issue) and will not be discussed here.

[1] In Australia, severe thunderstorms are defined as those that produce any of the following: hailstones with a diameter of 2 cm or more, wind gusts of 90 km $h^{-1}$ or greater, flash flooding, and tornadoes (BoM 1999).

** Current affiliation: Department of Atmospheric Science, University of Missouri—Columbia, Columbia, Missouri.

*Corresponding author address:* Dr. David M. L. Sills, Cloud Physics Research Division, Meteorological Service of Canada, King Weather Radar Research Facility, 14780 Jane St., King City, ON L7B 1A3, Canada.
E-mail: david.sills@ec.gc.ca

FDP forecasting and nowcasting issues associated with this event are further examined by Fox et al. (2004, in this issue) and Wilson et al. (2004, in this issue).

## 2. Background

Severe thunderstorms occur on a regular basis in NSW and are most common between the months of November and February (BoM 1999). The east coast of NSW is particularly susceptible to severe thunderstorms, and Sydney, with its high population density, is vulnerable to large amounts of damage. In fact, the Sydney area has experienced a number of significant severe thunderstorm events in recent times with extensive damage due to giant hail and violent winds (e.g., Mitchell and Griffiths 1993; BoM 1995, 1999). Many of these storms were intense supercells. The Sydney region also has the highest average annual tornado incidence in Australia at six per 26 000 km$^2$, though most tornadoes are usually weak and short lived (Geerts and Noke-Raico 1995).

The effect of boundaries, such as the sea-breeze and gust fronts, on thunderstorms in this region has received little formal attention. However, research in North America has shown that boundaries are preferred locations for convective initiation due mainly to enhanced lift, and can act to enhance the intensity of storms, including those that produce severe weather. Purdom (1976) used satellite imagery to show that intersecting boundaries often initiate intense convective development. Wilson and Schreiber (1986) found that 79% of storms in their study were initiated in association with radar-observed boundaries. This increased to 95% for storms with radar reflectivities of 60 dB*Z* or greater. Several recent field experiments have continued to examine the issue of convective initiation at boundaries (e.g., Sills et al. 2002; Weckwerth and Parsons 2002).

Boundaries are also known to have a large impact on the structure, duration, and movement of thunderstorms. The organization and motion of severe storms was found by Weaver (1979) to be influenced more by intense convergence at boundaries than by upper-level winds. Corfidi (1998) showed that mesoscale convective systems propagate in the direction of the greatest system-relative low-level convergence. This convergence is typically associated with a low-level jet but can also be provided by boundaries. Wilson and Megenhardt (1997), among others, have shown that a storm's organization and lifetime are greatly enhanced when storm motion is roughly equal to that of the storm's gust front.

Finally, it has been found that boundaries can provide the vorticity necessary for the development of rotation at low levels within a storm. Wakimoto and Wilson (1989) and Brady and Szoke (1989) showed that a thunderstorm without the persistent midlevel (~3–7 km AGL) mesocyclone that defines a supercell can produce a tornado by stretching vertical vorticity located along a *preexisting* boundary (i.e., one not generated by the storm itself). Maddox et al. (1980) also found preexisting boundaries to be a source of vertical vorticity for tornadic storms. In addition, they established that intense tornadoes associated with storms moving along or parallel to a boundary had longer lifetimes than those associated with storms moving across a boundary into cooler air.

With supercell thunderstorms, tornadoes are considered much more likely if the midlevel mesocyclone is accompanied by a separate low-level (~0–3 km) mesocyclone (Davies-Jones and Brooks 1993; Brooks et al. 1994). The way in which a thunderstorm develops a midlevel mesocyclone has been confirmed: low-level horizontal vorticity associated with strong environmental vertical wind shear is tilted by the storm's updraft (see Davies-Jones et al. 2001). However, research has pointed to the low-level environment in the vicinity of boundaries as the source of vorticity for low-level mesocyclones.

Numerical modeling studies have shown that a low-level mesocyclone develops when baroclinically generated horizontal vorticity, acquired by an air parcel moving along the cool side of a storm-generated boundary, is tilted and stretched by the storm updraft (e.g., Rotunno and Klemp 1985; Davies-Jones and Brooks 1993). Atkins et al. (1999) used a numerical model to simulate the evolution of supercell thunderstorms interacting with boundaries. They found that, when a preexisting boundary was present, air from the cool side of this boundary provided much of the horizontal vorticity necessary for low-level mesocyclogenesis, while the horizontal vorticity associated with storm-generated boundaries played only a minor role. Numerical modeling studies have also suggested a variety of methods by which tornadogenesis occurs following the development of the low-level mesocyclone, including a downward-building vortex via the ''dynamic pipe effect'' (Trapp and Davies-Jones 1997), two-celled vortex instabilities within the low-level mesocyclone (Rotunno 1986), and increasing mesocyclonic rotation that induces low-level convergence and intensifies vortex stretching (Wicker and Wilhelmson 1995).

Field observations tend to support the idea that preexisting boundaries are frequently the source of vorticity for low-level mesocyclones and subsequent tornadoes. Markowski et al. (1998) found that nearly 70% of significant supercell tornadoes during the 1995 Verification of the Origins of Rotation in Tornadoes Experiment (VORTEX; see Rasmussen et al. 1994) occurred near preexisting boundaries. Wakimoto et al. (1998), Rasmussen et al. (2000), Monteverdi et al. (2001), and Ziegler et al. (2001), among others, have also documented cases of tornadic supercell storms involving preexisting boundaries. Additional numerical modeling and observational studies are clearly needed to verify the theories related to low-level mesocyclogenesis and tornadogenesis described above.

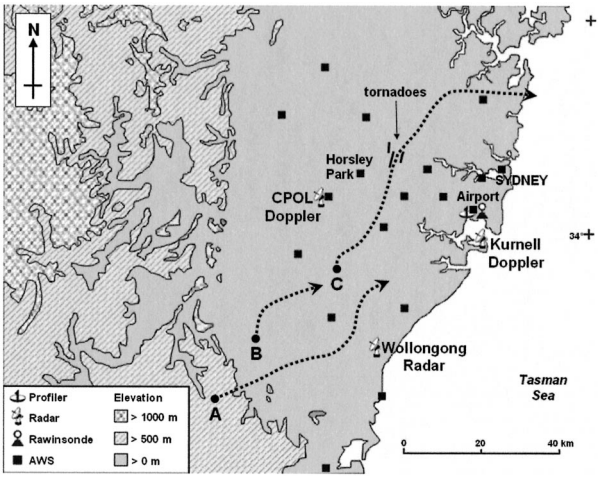


FIG. 1. Map of the Sydney region showing locations of instrumentation as well as tornado damage tracks and the paths of storms A, B, and C. The locations of 18 AWSs that were part of the FDP mesonet are shown.

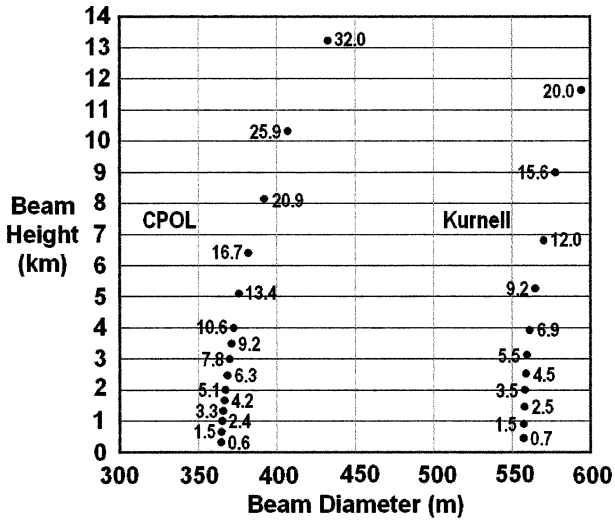


FIG. 2. Beam geometry for the C-Pol and Kurnell radars valid at 1600 LT, just prior to the development of tornadoes. Labels are elevation angles, given for each radar. The range used in the calculations is the distance from the radar to the center of rotation within the storm.

## 3. Data and methodology

### *a. Data sources*

The Sydney-area meteorological observation network was enhanced for the Sydney 2000 FDP. Instrument locations are shown in Fig. 1. Three Sydney-area radars were available. Two of these radars, the Kurnell radar and the C-band polarimetric radar (C-Pol), had Doppler capabilities while the Wollongong radar produced only reflectivity data. Table 1 compares radar characteristics and configurations for these radars. Beamwidth and height for the Doppler radars are shown in Fig. 2 valid at a time just prior to the development of tornadoes.

A dual-pulse repetition time (dual-PRT) scheme was used with the Kurnell radar. Details of this scheme are provided by May (2001). This scheme allows a considerable increase in the Nyquist (i.e., maximum unambiguous) velocity—in this case, from 13.4 to 40.0 m $s^{-1}$. However, it also introduces significant unfolding errors in regions of high azimuthal shear such as mesocyclones and microbursts. The Kurnell data were filtered in real time using a median filter in an attempt to correct these errors. This filter typically preserves real azimuthal gradients but suppresses local extrema. Using this scheme–filter combination, mesocyclone velocity signatures remained intact but the ability to detect tornadic signatures was severely reduced. For the C-Pol radar, this scheme was not applied and data filtering was minimized to increase the radar's ability to detect boundaries in optically clear air.

Several different radar display and analysis systems were used during the FDP. These included Auto-nowcaster (ANC) developed by the National Center for Atmospheric Research (NCAR), the Canadian Radar Decision Support (CARDS) system of the Meteorological Service of Canada (MSC), and the Warning Decision Support System (WDSS) from the National Severe Storms Laboratory (NSSL). An overview of these systems and how they were used during the FDP is provided by Keenan et al. (2002). The radar data in this paper are presented using images rendered by these systems, some of which were used by FDP and Australian Bureau of Meteorology (BoM) forecasters during the project.

Surface measurements were made from a local mesonet of 29 stations. The 18 automated weather stations (AWSs) shown in Fig. 1 measured 10-m winds, 1.2-m temperature and humidity, barometric pressure, and precipitation amount. Most of these stations produced av-

TABLE 1. Comparison of the characteristics of the three radars available during the FDP. Note that the higher Nyquist velocity for the Kurnell radar is due to the use of a dual-pulse repetition time scheme as described in the text.

| | Kurnell | C-Pol | Wollongong |
|---|---|---|---|
| Wavelength (cm) | 5 (C band) | 5 (C band) | 10 (S band) |
| Beamwidth (°) | 1.0 | 1.0 | 2.0 |
| Range bin size (m) | 250 | 300 | 1000 |
| Effective range (km) | 110 | 110 | 220 |
| Scan cycle (bottom up, min) | 5 | 10 | 10 |
| Scan angles (°) | 11 | 15 | 15 |
| Nyquist velocity (m $s^{-1}$) | 40.0 | 13.4 | — |

eraged data every minute while others had half-hourly and hourly observations. The remaining stations, with locations along the shore of Sydney Harbour, measured 10-m winds only. For the FDP, up to four radiosonde launches were made per day at 0600, 1000, 1500, and 2200 LT (LT = UTC + 11 h). The balloons were launched from Sydney International Airport (see Fig. 1 for location).

Visible, infrared, and water vapor channel satellite images from Japan's *Geostationary Meteorological Satellite-5* (*GMS-5*) were available during the FDP, though at irregular intervals. Sea surface temperature maps provided by the BoM used data from the Advanced Very High Resolution Radiometer on board the United States National Oceanic and Atmospheric Administration series of polar-orbiting satellites.

The Variational Doppler Radar Analysis System (VDRAS; see Crook and Sun 2001), a high-resolution analysis system for the assimilation of radar, surface, and profiler data, was implemented for the FDP and ingested data from the two Doppler radars, the 29-station mesonet, and a 54.1-MHz wind profiler at Sydney International Airport. This analysis system used cost function minimization to find a model solution fitting the observational data as closely as possible. The numerical model consisted of the dry, anelastic, incompressible equations of motion on a grid with 3-km horizontal spacing and 400-m vertical spacing. Output from this system included near-surface (nominal height 100 m) two-dimensional winds over the FDP region every 10 min as well as derived fields such as horizontal divergence.

Photographs and video of the storms were taken by several project participants and area residents. The lead author took a series of photographs from the BoM weather office in a high-rise building near downtown Sydney as the event unfolded. G. Nagle photographed the event from a high-rise building in Parramatta, just a few kilometers from the tornadoes. A number of photographs and video sequences were also shot by storm chaser M. Smith.

Finally, a damage survey was conducted in the days following the event. The survey results, when combined with the photograph and video records, provided important evidence for storm evolution, tornado occurrence and timing, and damage intensity.

### *b. Boundary identification*

Reflectivity imagery from the Doppler radars was the primary source of data for boundary detection since various boundaries were made visible by reflectivity ''fine lines'' in optically clear air. The locations and movements of boundaries discussed in subsequent sections of this paper were based on careful manual analysis of fineline structures using loops of individual plots of low-level reflectivity data from both C-Pol and Kurnell radars. Mesonet and wind profiler data were used to support the existence of the radar-identified boundaries and characterize the low-level environment on either side. Visible channel satellite images were used, when available, to confirm the origins and locations of boundaries.

### *c. Mesocyclone identification*

Radial velocity data from the C-Pol and Kurnell radars were used to identify patterns of divergence and shear in the wind field as well as the intensity of these features. Mesocyclones were manually identified in the radar dataset using the Rankine-combined vortex model.[2] For the purposes of this study, a velocity couplet was considered to represent some part of a mesocyclone if

- the maximum differential velocity (MDV) exceeded 20 m $s^{-1}$,
- the vortex core diameter (the distance between the couplet's velocity maximum and minimum) was between 2 and 10 km wide, and
- a similar velocity couplet exceeding the MDV threshold of 20 m $s^{-1}$ was present on at least one adjacent scan angle *and* on either a previous or subsequent scan (to ensure spatial and temporal continuity).

To allow for convergent (divergent) vortices in the lower (upper) portions of the mesocyclone, the inbound and outbound velocity maxima used to calculate MDV did not have to be at the same range from the radar.

## 4. The prestorm environment

### *a. Synoptic-scale forcing*

On 3 November, the synoptic-scale environment over the eastern third of Australia was characterized by a weak pressure trough that extended from the upper troposphere to the surface (Figs. 3a and 3b). The surface trough axis, indicated in Fig. 3a, moved slowly eastward and reached eastern NSW late in the day. Figure 3b shows that the upper-level jet stream was located well away from the Sydney area. However, upper-level winds veered (i.e., changed direction in a clockwise sense) and increased in strength slightly as the trough approached. Morning satellite imagery (not shown) indicated mainly cloudless skies over NSW with the exception of a north–south-oriented band of cloud and a few showers over extreme eastern sections. Most of this cloud moved east over the Tasman Sea by afternoon, leaving the Sydney region under fair skies. Overall, synoptic-scale forcing was weak over NSW and the Sydney region.

[2] The Rankine-combined vortex has a tangential velocity equal to $V \cdot R \cdot r^{-0.5}$ for $r > R$ and $V \cdot R^{-1} \cdot r$ for $r \leq R$, where $r$ is the distance from the center of the vortex and $V$ is the peak tangential velocity occurring at core radius $R$.

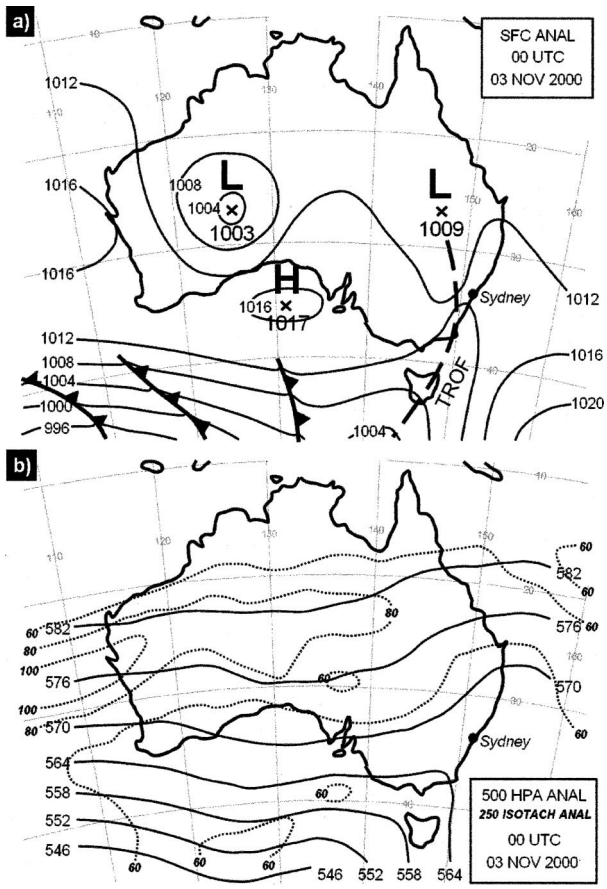


FIG. 3. Australian (a) surface and (b) 500-hPa analyses at 1100 LT (0000 UTC) 3 Nov. The surface analysis shows isobars contoured every 4 hPa as well as the positions of pressure centers, fronts, and troughs. The 500-hPa analysis shows geopotential heights contoured every 6 dam and 250-hPa isotachs at 20-kt intervals for winds ≥60 kt (31 m s$^{-1}$). Analyses adapted from BoM operational products.

### b. The sea breeze

Maximum inland surface air temperatures ranged between 23° and 27°C while surface dewpoint temperatures ranged from 14° to 18°C. Sea surface temperatures off the coast of Sydney, at around 20°C, were several degrees lower than the maximum inland air temperatures, indicating that the development of the sea breeze, a common feature in this coastal region, was possible. In fact, the leading edge of the sea breeze, known as the sea-breeze front (SBF), was identified moving inland from the coast using data from the mesonet and the Doppler radars. It moved onshore near 1100 LT and traveled as far as Horsley Park (see Fig. 1 for location), approximately 40 km inland, by 1500 LT. The arrival signature in the mesonet data was quite subtle due to the influence of the large-scale onshore flow. In most cases, there was little or no change in temperature or dewpoint across the SBF, though changes in the character of the wind were evident. Data from the Horsley Park mesonet station are shown in Fig. 4 and illustrate the arrival of the sea breeze most clearly. There was a rapid shift in wind direction from north to east, an increase in maximum wind speed, and a large (~2°C) positive spike in both temperature and dewpoint as the SBF reached the station near 1449 LT. Once the front had passed, temperatures (dewpoints) returned to values slightly lower (higher) than those before the arrival of the sea breeze.

### c. Buoyancy and shear

Radiosondes were launched from Sydney International Airport at 1000 and 1500 LT. The 1500 LT radiosonde was launched about an hour before tornadoes developed. However, it flew through cumulonimbus over much of its flight, resulting in considerably altered thermodynamic and wind profiles above 3 km. Therefore, a proximity sounding[3] was constructed by modifying the 1000 LT sounding using surface data from the Horsley Park mesonet station near maximum daytime heating at 1500 LT. The station was in the path of the storm, and in modified sea-breeze air just to the east of the SBF, at that time. The resulting thermodynamic and wind profiles are shown in Fig. 5.

The proximity sounding possessed a deep, moist layer below 600 hPa with a considerably drier layer above. A parcel mixed through the lowest 50 hPa was lifted using the virtual temperature correction suggested by Doswell and Rasmussen (1994). The resulting convective available potential energy (CAPE) was 995 J kg$^{-1}$ with no convective inhibition (CIN) present. The wet-bulb 0°C height was 2750 m. Wet-bulb 0°C heights between 2100 and 2800 m are used operationally in NSW to indicate the potential for large hail. Temperature and dewpoint data below 3 km from the 1500 LT sounding are superimposed in Fig. 5 and show that the lower portions of the atmosphere at 1500 LT were similar to that of the proximity sounding, except for the prominent surface-based inversion due to the relatively unmodified sea-breeze air at the airport location.

Proximity sounding winds were relatively light through the entire troposphere ranging between 3 and 12 m s$^{-1}$. A notable feature was a shallow (<1 km) layer of easterly to northerly winds that was located beneath a deep layer of mainly westerly winds. This feature had persisted for several days, allowing the depth of available moisture to increase, and was enhanced by the sea breeze later in the day. The associated ground-relative hodograph is shown in Fig. 6. There was considerable curvature in the lowest 2 km while winds aloft were quasi unidirectional. The 0–6-km bulk (total) shear was found to be 11.3 m s$^{-1}$ (33.5 m s$^{-1}$). Observational (e.g., Bunkers et al. 2000) and modeling (e.g., Weisman

[3] A proximity sounding using observations made several hours before storm development may not accurately represent the tornadic environment. See Brooks et al. (1994) for a detailed discussion of the problems with proximity soundings.

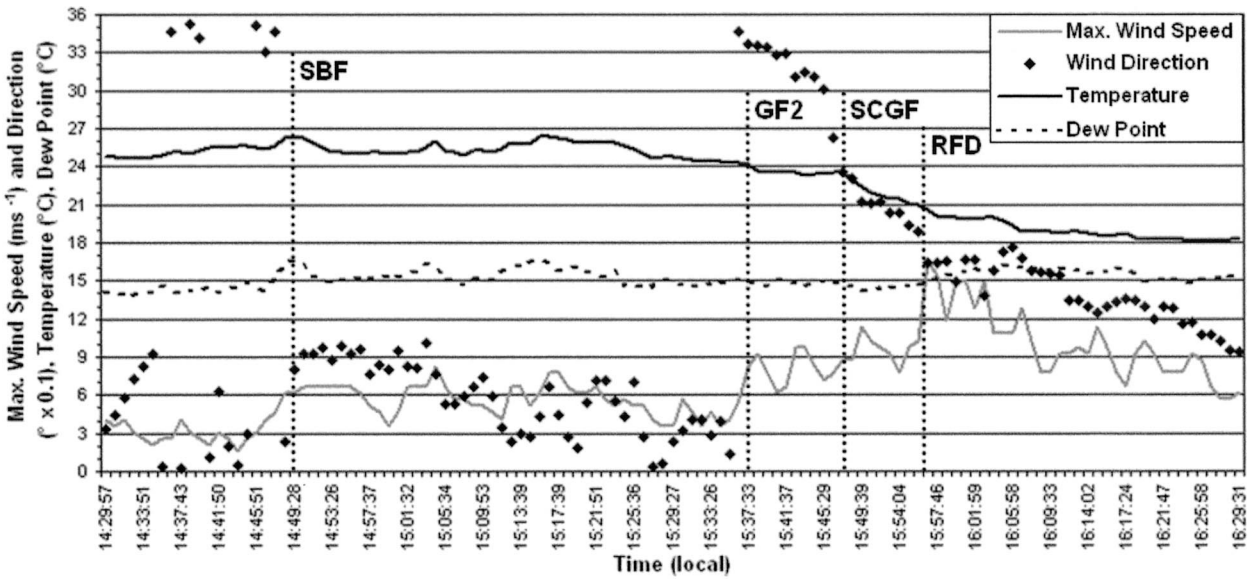


FIG. 4. Horsley Park AWS 1-min data showing the arrival of the sea-breeze front (SBF), a gust front from a thunderstorm to the northwest (GF2), the storm C gust front (SCGF), and the storm C rear-flank downdraft (RFD).

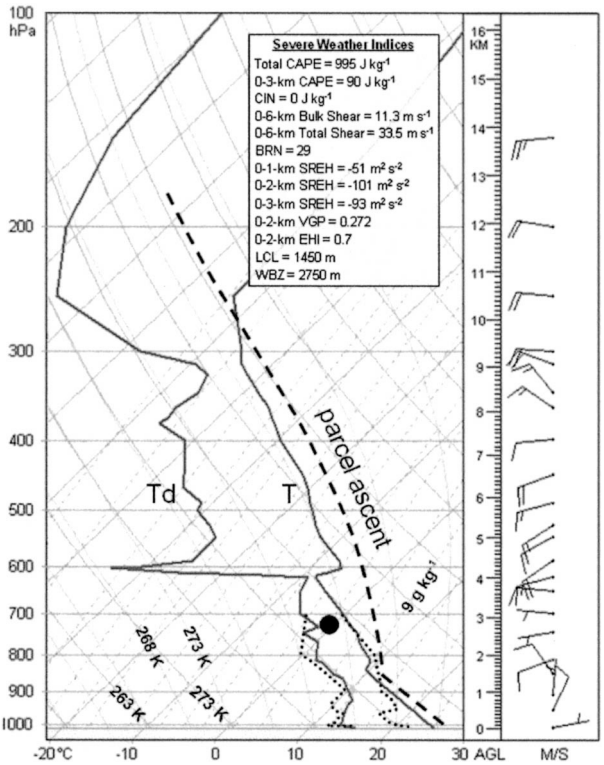


FIG. 5. Proximity sounding plotted on a skew *T*–log*p* diagram with data from Sydney International Airport at 1000 LT modified using surface observations from the Horsley Park AWS at 1500 LT. Temperature and dewpoint curves (labeled solid lines) are in °C. Selected wind data are in m s$^{-1}$ (short barb, 2.5 m s$^{-1}$; long barb, 5.0 m s$^{-1}$). Dashed line is ascent curve using the virtual temperature correction for a parcel mixed through the lowest 50 hPa. Dotted lines are low-level temperature and dewpoint data from the 1500 LT sounding. Black circle indicates the wet-bulb 0°C height. Various severe weather indices are also provided.

and Rotunno 2000) studies have found that 0–6-km bulk (total) shear values of at least 10–15 m s$^{-1}$ (20–25 m s$^{-1}$) are required for the development of supercell thunderstorms. In addition, the bulk Richardson number

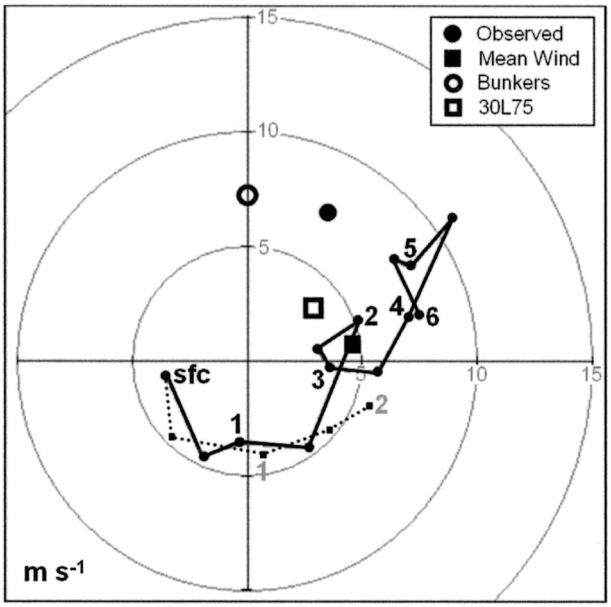


FIG. 6. Ground-relative proximity hodographs with data from Sydney International Airport at 1000 LT (solid line to 6 km AGL) and 1500 LT (dashed line to 2 km AGL) modified using the surface wind from the Horsley Park AWS at 1500 LT. Data points are provided every 500 m with labels every km and at the surface. The WDSS-derived average motion of the tornadic storm (dark circle), 0–6-km mean wind (dark square), Bunkers storm motion (open circle), and 30L75 storm motion (open square) are indicated. Wind speed in m s$^{-1}$.

(BRN) calculated using the proximity sounding data was 29. BRN values between 15 and 45 are used operationally in NSW to delineate supercell potential, based on the results of Weisman and Klemp (1984).

The 0–6-km thickness-weighted mean wind and the observed storm motion for the tornadic storm were 261° at 4.6 m $s^{-1}$ and 209° at 7.3 m $s^{-1}$, respectively, as shown in Fig. 6. The observed storm motion is the mean of 5-min-average storm motions diagnosed by WDSS during the period when a mesocyclone was present with the tornadic storm. Clearly, the tornadic storm moved faster than, and well to the left of, the mean wind. Storm-relative environmental helicity (SREH) calculated for the 0–2-km layer using the observed storm motion gave $-101$ $m^2$ $s^{-2}$ (negative in the Southern Hemisphere). In addition, SREH calculated using 0–2-km wind data from the 1500 LT sounding and Horsley Park surface wind data at 1500 LT (superimposed in Fig. 6), as well as the observed motion of the tornadic storm, gave a value of $-106$ $m^2$ $s^{-2}$. A value of $-100$ $m^2$ $s^{-2}$ is used operationally by the BoM as the lower threshold for supercell development. Operational experience in the United States also suggests that supercells can occur with SREH values (positive in the Northern Hemisphere) between 100 and 150 $m^2$ $s^{-2}$ (Moller et al. 1994). However, it is thought that considerably higher values are typically needed for the development of strong low-level mesocyclones and significant supercell tornadoes (Davies-Jones et al. 1990).

### *d. Storm type and intensity*

Analysis of the proximity sounding suggests that ample instability and low-level moisture were available for the formation of thunderstorms. Lift could be provided via mesoscale circulations such as the sea-breeze front and, to a lesser extent, the trough at the synoptic scale. Deep-layer shear and BRN values calculated using the proximity sounding data were within range for the formation of supercells, though SREH values indicated only marginal support for the development of significant supercell tornadoes. Large hail and downdraft-related wind gusts appeared to be the greatest severe weather threats due to the favorable wet-bulb freezing level and the abundance of dry air aloft, respectively.

The BoM severe weather outlook from the morning of 3 November indicated that severe thunderstorms were possible over much of eastern NSW and bulletins were issued to that effect (see Fox et al. 2004). The forecasters, however, felt that the risk was lower in the Sydney region since it appeared that storm organization would be insufficient for the strongest storms to persist while moving from higher terrain to the coastal plain.

## 5. Storm description and evolution

This section describes the storms of 3 November and their evolution in detail. First, the tornadoes and associated damage are discussed with the aid of photographs and maps. Second, boundaries and the development and structure of thunderstorms are described using reflectivity images and mesonet data. Third, the mesocyclones and tornadoes associated with the tornadic storm are examined using radial velocity images from both the C-Pol and Kurnell radars. The reader is reminded that, in the Southern Hemisphere, mesocyclones and cyclonic tornadoes rotate in a clockwise fashion when viewed from above.

### *a. Storm and damage description*

The BoM received numerous reports of severe weather in the Sydney region between 1445 and 1700 LT, including hail up to the size of golf balls (~4 cm), heavy rain accompanied by flash flooding, damage to buildings and trees, and rotating clouds and tornadoes. A storm damage survey revealed three distinct tornado damage tracks, each having a maximum path width of about 200 m, approximately 25 km west of downtown Sydney (Fig. 7). The South Wentworthville and Pendle Hill tornadoes (hereafter tornado S and tornado P, respectively) had pathlengths near 1.5 km and light damage consistent with a value of F0 on the Fujita scale (Fujita 1981). The tornado in Greystanes (hereafter tornado G) had a pathlength near 3 km and caused mainly F0 damage, though F1 damage, mainly to a house, was found near the end of its track. Cyclonic rotation could only be confirmed for tornado S and tornado G. At Ringrose Primary School, shown in Fig. 7 between tornado tracks S and G, the roof was removed from a school building and debris flew westward into a nearby electrical substation. This damage was isolated and did not appear to be tornado related. The survey team also obtained a report of cricket-ball-sized hail (7 cm) that fell approximately 6 km south of the area affected by tornadoes.

The first visual evidence of a tornado was a faint funnel cloud and column of dust and debris beneath the northern part of a large wall cloud in a photograph taken at 1603 LT (Fig. 8a). A number of additional photographs of the tornado and wall cloud were taken as the tornado moved toward the north-northeast and dissipated near 1613 LT (Figs. 8b–d). These photographs show that the northern part of the wall cloud became completely surrounded by the rear-flank downdraft (RFD) induced clear slot approximately 10 min after the tornado developed. The tornado appears to be located at the boundary between the RFD air (clear slot) and the updraft air (wall cloud), on the eastern periphery of the wall cloud.

Figure 8e is a photograph taken facing east at 1621 LT that depicts a wall cloud (believed to be the southern part of the larger wall cloud) moving across the Western Motorway (M4) near Ettalong Road. This is the location of the Greystanes F1 tornado damage (see Fig. 7). A bit of low-hanging cloud rotating beneath the wall cloud was reportedly associated with the tornado. Figure 8f

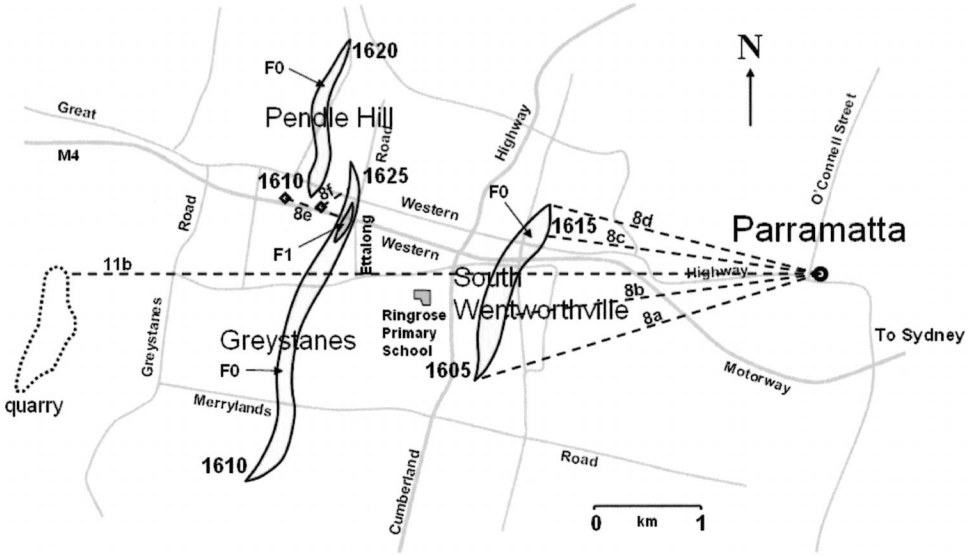


FIG. 7. Tornado damage track map showing the paths of the three tornadoes, the associated damage intensities on the Fujita scale, the estimated tornado start and end times (LT), and the viewing direction (dashed lines with references to figure numbers) for photographs by M. Smith (diamonds) and G. Nagle (circle).

provides a view of these features at 1624 LT just north of the M4. The photographer noted that the tornado appeared to dissipate near this time, in agreement with the end of the tornado G damage track.

### *b. Storm structure and boundaries*

Sydney-area radars began to detect convective precipitation just before 1100 LT on 3 November. Scattered showers and thunderstorms were first initiated along the Blue Mountain range west of Sydney, most likely due to preferential heating of the eastern sides of the mountains. They then drifted eastward across the coastal plain, as often occurs in this region (Potts et al. 2000). One of the first of these showers and thunderstorms to reach the SBF southwest of Sydney near 1320 LT (hereafter storm A) rapidly increased in intensity. The storm moved in a more northerly direction after developing both mid- and low-level rotation, indicating a transition to supercell processes. Figure 9a shows storm A at 1340 LT undergoing rapid intensification with a northward-moving gust front in its wake.

Another strong thunderstorm (storm B) was initiated approximately 20 km to the west of storm A at 1400 LT near the location where the SBF and the storm A gust front intersected. Only very weak rotation was detected with storm B. A report of 24 mm of rain in 8 min was received that was associated with storm A while one report of 2-cm hail was received associated with storm B. Figure 9b shows storms A and B at 1430 LT as well as three well-defined boundaries: the storm A–B gust front, the SBF, and a gust front approaching from the northwest (hereafter GF1). Storm A had a well-defined weak echo region (WER) on its left flank at this time, as did storm B. A hook-shaped reflectivity appendage was also present with storm A.

Storm C formed near 1500 LT at the location where GF1, the SBF, and the storm A–B gust front interacted, roughly 10 km northeast of storm B. The first reports of 4-cm-diameter hail were received shortly after this time as storm C rapidly intensified, developing a bounded weak echo region (BWER) to 7 km in height, and storms A and B began to dissipate. Figure 9c shows the situation at 1510 LT. The gust front associated with outflow from storms A, B, and C formed a great arc gradually expanding northward and westward (only partially shown in the figure). North of storm C, this gust front (hereafter referred to as the storm C gust front, SCGF) intersected with the SBF forming what is often referred to as a triple point [since the boundaries separate three air masses; see Weiss and Bluestein (2002)]. In addition, another thunderstorm gust front approaching from the northwest (hereafter GF2) began to intersect the SBF roughly 30 km north of storm C. Temperature and dewpoint observations made at mesonet stations near the triple point and GF2 are shown in Fig. 9c and indicate the differences between these air masses.

Between 1520 and 1530 LT, the SCGF began to push out ahead and to the north of storm C while storm C, rapidly developing midlevel rotation, began tracking to the northeast. This increased the distance between the triple point and the storm C updraft region. However, new convective development began on the northwest flank of storm C along the SCGF in the direction of the triple point, resulting in an appendage-shaped echo there. This feature, shown at 1530 LT in Fig. 9d, was


FIG. 8. Images showing storm features at (a) 1603, (b) 1608, (c) 1612, (d) 1613, (e) 1621, and (f) 1624 LT. Yellow lines outline the funnel cloud and red lines outline the dust and debris cloud. Photographs (a)–(d) were taken by G. Nagle. Photograph (e) and video capture (f) were taken by M. Smith. What appears to be airborne debris in (f) is actually raindrops on the vehicle windshield. Viewing directions are illustrated in Fig. 7.

associated with only very weak low-level rotation. For a brief period, a WER and weak midlevel rotation were present on both the new and the old left flanks of storm C. Gradually, the new updraft region became dominant and the old updraft region dissipated—a regenerative process that appears to be similar to that described by Weisman and Klemp (1986). Low-level reflectivity increased rapidly and further reports of hail to 4 cm in diameter and heavy rain were received by the BoM at 1530 LT. GF2 continued to interact with the SBF and was approaching the triple point, located roughly 15 km northwest of the storm's updraft region. The VDRAS

200-m horizontal convergence field at this time (not shown) indicated a global maximum near $1.5 \times 10^{-3}$ $s^{-1}$ in the vicinity of the triple point.

The SBF, which had moved gradually westward up to this time, was forced eastward by GF2 beginning at 1535 LT so that the triple point began to move toward the storm C updraft region. The BWER collapsed at 1540 LT, though Kurnell radar data show that a new and pronounced BWER to 9 km in height developed within storm C near 1545 LT. This marked the beginning of the mature phase of storm C following updraft regeneration.

C-Pol radar data indicate that, by 1550 LT, the SCGF and the SBF/GF2 were beginning to wrap around the reflectivity appendage at the left flank of storm C, resulting in the intersection point of these boundaries laying beneath the updraft region of the storm. Both mid- and low-level mesocyclones had developed. The BWER, as illustrated using WDSS images in Fig. 10, reached its maximum height of 11 km as this occurred. Reports were received at this time of hail up to 4 cm in diameter as well as hail of unknown size causing damage to cars in the storm C area.

At 1600 LT, the BWER had decreased in height to 8 km, signaling the beginning of updraft collapse. A pronounced hook echo was apparent in the low-level reflectivity data, as shown in Fig. 9e. At the same time, a strong gust of wind associated with a new RFD pulse began to pick up dust (source estimated to be a quarry; see Fig. 7 for location) and loft it into the air. Much of it reentered the cloud base to the north and resulted in the development of a lowering there. This dust plume was captured in a photograph taken facing west at 1602 LT (Fig. 11a). A wall cloud, tail cloud, and inflow bands are also apparent. A photograph taken facing nearly the same direction (and considerably closer to the area of interest) at 1604 LT shows a wall cloud to the left with a clear slot developing south of the dust plume (Fig. 11b). The bases of a line of cumulus along the SCGF can be seen extending to the west. The Horsley Park mesonet station, located roughly 8 km southwest of the quarry, reported a wind gust of more than 16 m $s^{-1}$ as the RFD air arrived (see Fig. 4). This was the largest surface wind gust recorded by the FDP mesonet stations on this day.

Photographic evidence and radar data suggest that tornadoes began to occur in the vicinity of the wall cloud near this time. In addition, both radars indicated a boundary intersecting the SCGF and extending north of storm C, as shown in Fig. 9e. Kurnell radar data (not shown) also suggest a second boundary moving eastward past the storm C updraft region and beyond. It is believed that these boundaries are the SBF and GF2, respectively, though this is difficult to confirm with the available data (the positions of these boundaries are marked in Figs. 9e and 9f with dashed lines to reflect this uncertainty). It is likely that the westward surge of the SBF was caused by outflow from a thunderstorm initiated to the north of storm C near the estimated position of the SBF. Wilson and Megenhardt (1997) described a similar process that occurs with the west coast sea breeze on the Florida peninsula where outflow from storms initiated along the west coast sea breeze assists the eastward movement of the sea-breeze front.

By 1610 LT, the radars showed that the storm C BWER had decreased in height to 6 km. Low-level reflectivity reached a maximum (>60 dBZ) at this time and the hook echo continued to be pronounced. It is likely that giant hail was falling based on the locations of both high radar reflectivities and the location of 7-cm hail obtained via damage survey interviews. The hook echo and BWER associated with storm C dissipated by 1620 LT though a WER was still present, and large hail to 4-cm diameter continued to be reported. As storm C moved northeastward, the SBF continued to push westward with the triple point moving northwestward away from storm C's updraft region. In addition, GF2 continued to move eastward.

Storm C briefly reintensified at 1630 LT producing a BWER to 6 km in height. Fine lines in the C-Pol reflectivity data showed the triple point roughly 10 km northwest of the updraft region of storm C and continuing to move away from the storm. Reflectivity data also suggest deformation of the low-level echoes along the northern edge of storm C due to GF2, as suggested in Fig. 9f. The BWER collapsed for a final time after 1640 LT but a mesocyclone persisted until 1700 LT. After 1700 LT and the demise of the mesocyclone, the deviate motion of storm C ceased and the remnants of the storm began to drift east toward the Tasman Sea.

Additional showers and thunderstorms were initiated at the SCGF as it pushed northward and westward, including a strong thunderstorm at 1740 LT. However, no further reports of severe weather in the Sydney region were received.

### *c. Storm C mesocyclones and tornadoes*

Storm C developed a midlevel mesocyclone and a low-level mesocyclone prior to tornadogenesis. Their intensity and depth with time are depicted in Fig. 12 using unfolded radial velocity data from the C-Pol radar. A midlevel mesocyclone having a core diameter near 7 km first appeared in the C-Pol velocity data at 1530 LT. MDV values ranged from 28.2 to 37.3 m $s^{-1}$ at this time. This midlevel mesocyclone intensified and appeared to descend between 1530 and 1550 LT, with maximum MDV values reaching 43.1 m $s^{-1}$.

A low-level mesocyclone first appeared in the C-Pol velocity data at 1550 LT, extending from the surface to about 3 km,[4] beneath the western periphery of the mid-

[4] At 1550 LT, the outbound half of the velocity couplet was revealed via clear-air radar returns in the lowest 1 km. Not enough clear-air returns were available on the outbound side of the couplet between 1 and 2.5 km to properly determine MDV values, though the mesocyclone was present through this layer.

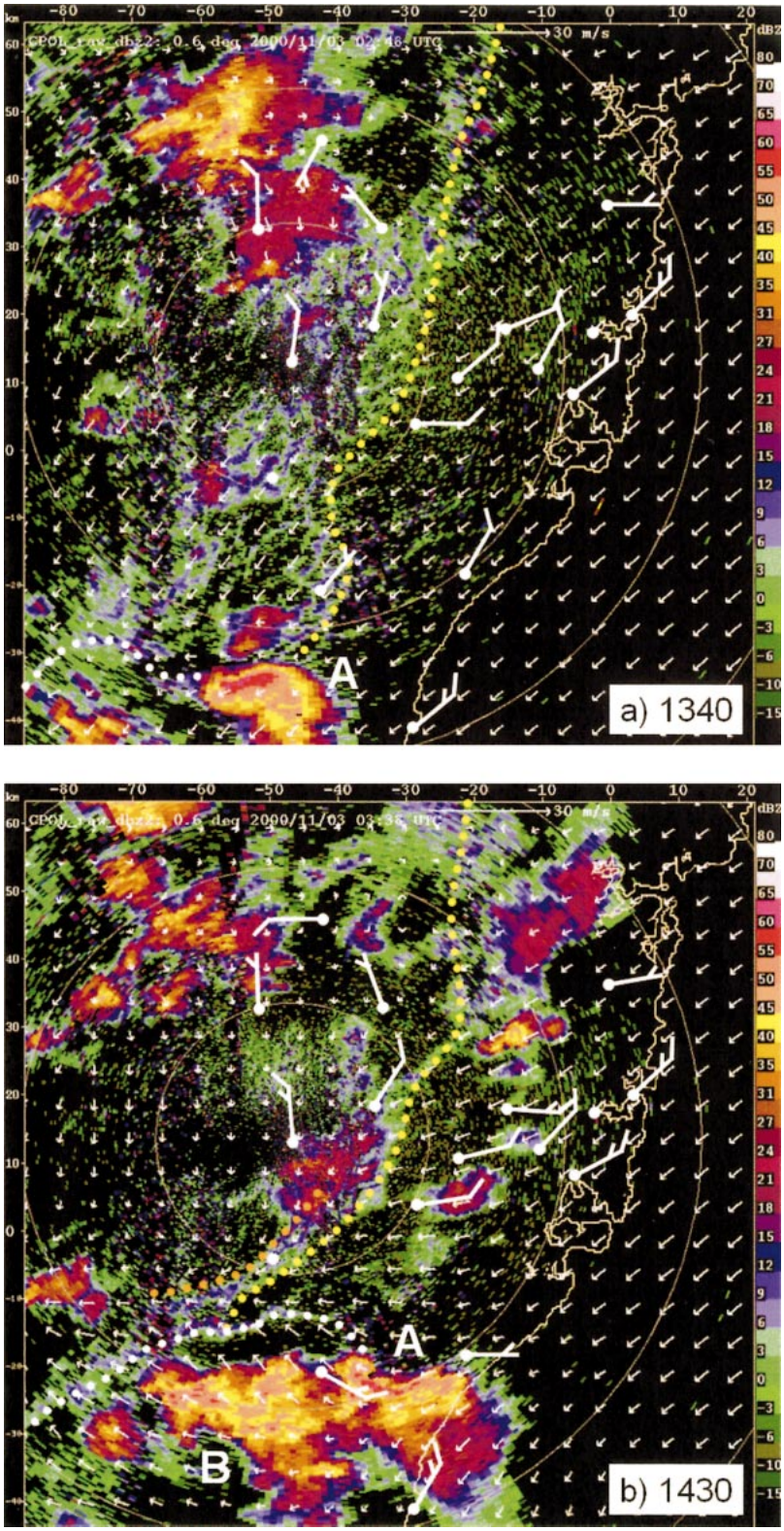


FIG. 9. ANC composite images at (a) 1340, (b) 1430, (c) 1510, (d) 1530, (e) 1600, and (f) 1630 LT. Radar reflectivity is from the C-Pol 0.6° scan. VDRAS 100-m winds in m $s^{-1}$ are superimposed (scale at top of each image). The boundaries are labeled as follows: SBF (dotted–dashed yellow line), storm A–B–C gust front (dotted white line), GF1 (dotted

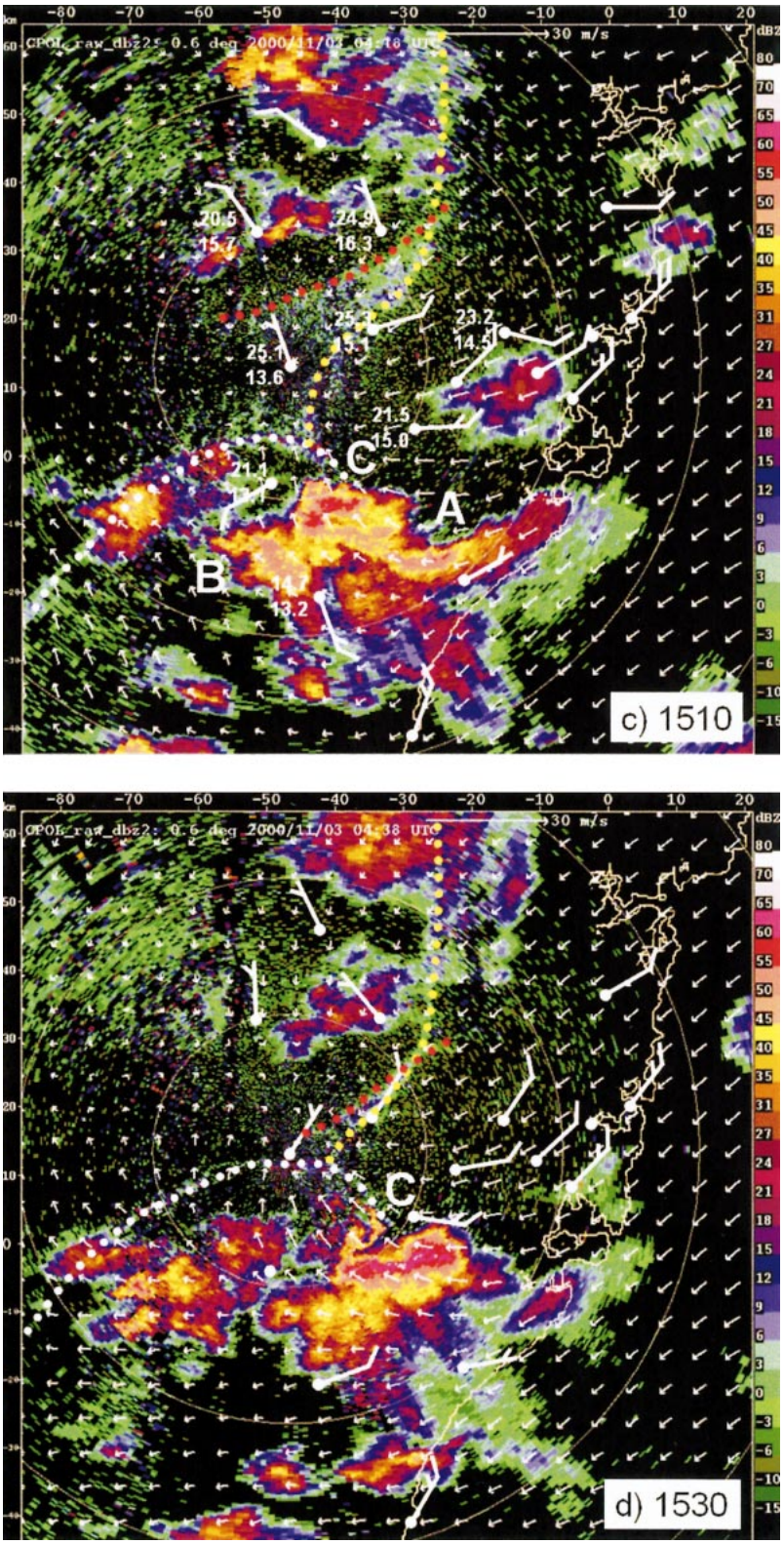


FIG. 9. (*Continued*) orange line), and GF2 (dotted–dashed red line). Storms A, B, and C are labeled. Mesonet temperature and dewpoint data are provided at 1510 LT. Mesonet winds are in m s$^{-1}$ (short barb, 2.5 m s$^{-1}$; long barb, 5.0 m s$^{-1}$). Only mesonet data within $\pm$10 min of nominal time are provided.

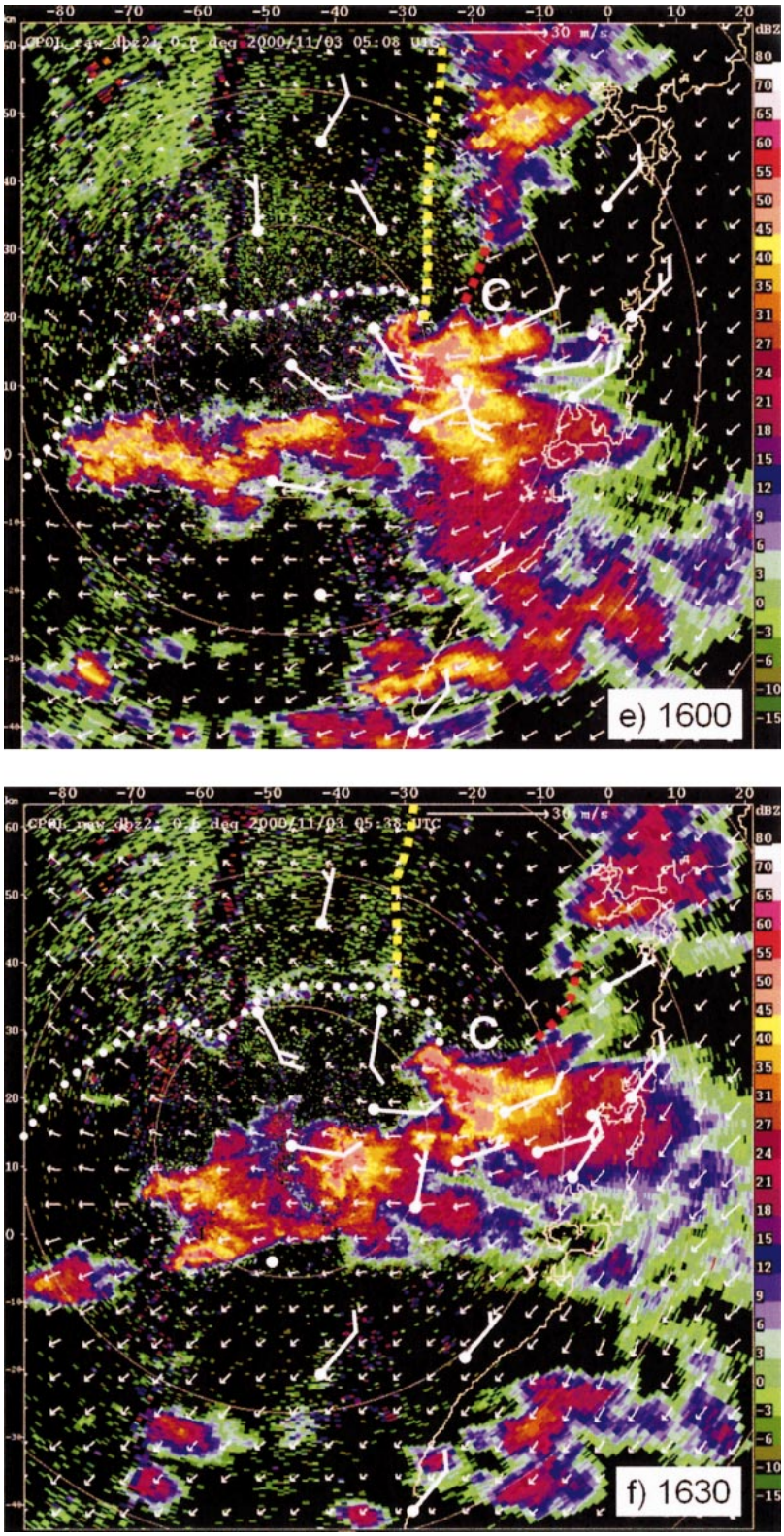


FIG. 9. (*Continued*)

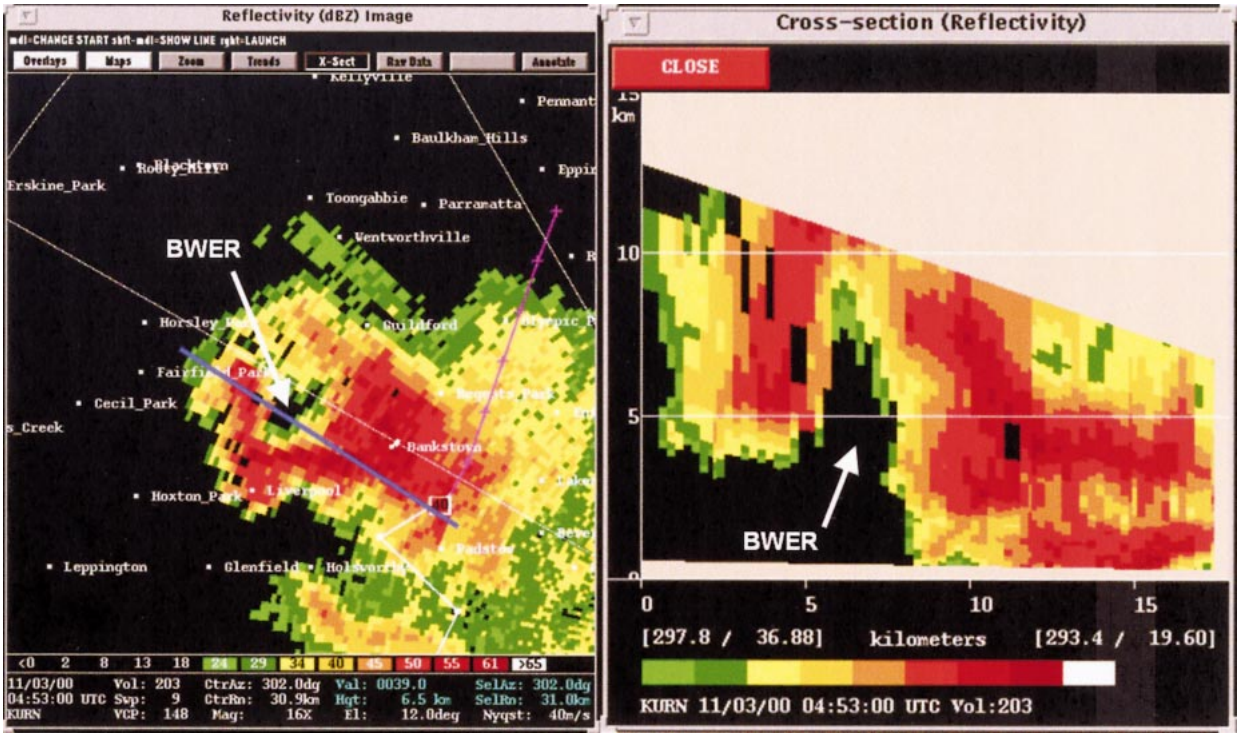


FIG. 10. WDSS image from Kurnell radar at 1550 LT showing a plan view (12.0° elevation angle) of the storm C BWER at left and a vertical cross section through the BWER at right. The cross section is drawn along the blue line shown in the plan view. White and magenta lines in the plan view show the past and forecast tracks of storm C, respectively. The reflectivity scale is shown at bottom left of the plan view.

level mesocyclone. The low-level mesocyclone had a core diameter near 7 km with the greatest MDV near the surface at 29.1 m $s^{-1}$. The formation of the low-level mesocyclone at this time is supported by photographs taken by the lead author (not shown) that indicate the rapid development of a wall cloud and tail cloud beneath storm C between 1556 and 1600 LT. Wakimoto and Liu (1998) have shown that a rotating wall cloud is a visual manifestation of the low-level mesocyclone.

The updraft center at 1550 LT, as indicated by the position of the BWER, was located on the southeastern half of the low-level mesocyclone with downdraft air dominating the northwestern half. A similar pattern appeared to exist for the midlevel mesocyclone. Such ''divided mesocyclones'' are described by Lemon and Doswell (1979). The updraft center was also located on the cool side of the SBF. Inflow bands photographed near this time (see Fig. 11a) clearly indicate air moving into the updraft region of the storm from the northeast. This suggests that at least some of the air ingested by the storm was modified marine air originating from over the Tasman Sea.

At 1600 LT, only a few minutes prior to the development of the first tornado, rotation intensified through the depth of the storm, as shown in Fig. 12. MDV values ranged from 30.2 m $s^{-1}$ at 750 m to 48.2 m $s^{-1}$ at 5 km. A secondary MDV maximum was apparent near 1.5 km. Radial velocity data at this time from both the C-Pol and Kurnell radars at heights of 0.5, 2.0, 4.0, and 6.5 km AGL are shown in Fig. 13. The C-Pol data indicate strong convergent rotation at 0.5 km gradually changing to strong divergent rotation at 6.5 km. Due to the presence of large hail within the storm, Kurnell data below 3 km suffer from severe attenuation and sidelobe contamination and show only part of the low-level mesocyclone. However, the midlevel mesocyclone begins to appear at 4 km and is well defined at 6.5 km.[5]

At 1610 LT, the mesocyclones began to decrease in intensity and the nature of their vorticity appeared to change. As shown in Fig. 14, three areas of enhanced azimuthal shear developed, embedded within the larger circulation and having core diameters near 3 km. Two areas, located over tornado tracks P (MDV = 29 m $s^{-1}$, 0.6°) and S (MDV = 27 m $s^{-1}$, 4.2°), had the greatest shear near the surface while the third area, located over tornado track G (MDV = 27 m $s^{-1}$, 10.6°), had the greatest shear near the midlevels of the storm. The tornadoes on this day, with diameters near 200 m as sug-

[5] The Kurnell data at 6.5 km appear to suggest a tornado vortex signature (TVS; see Brown et al. 1978) located a few kilometers east of the tornado tracks. This region of strong gate-to-gate shear has spatial and temporal continuity. However, such a feature could not be found in the C-Pol data and further investigation has shown that it is most likely an artifact resulting from the use of the dual-PRT scheme with median filtering.

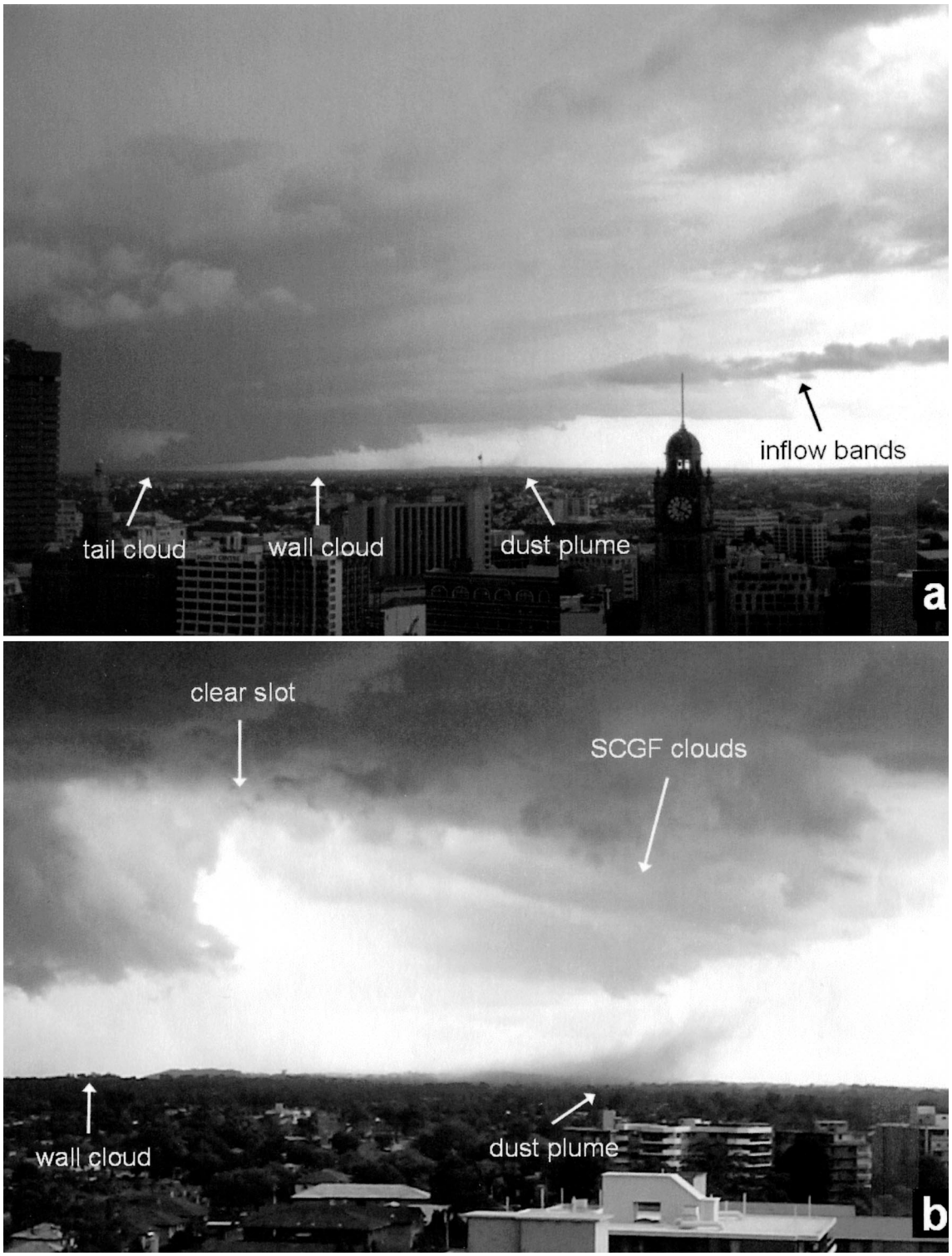


FIG. 11. Photographs of the storm C wall cloud and RFD dust plume (a) by the lead author at 1602 LT and (b) by G. Nagle at 1604 LT, both facing west. The distance to the dust plume is estimated at 28 km for (a) and 7 km for (b).

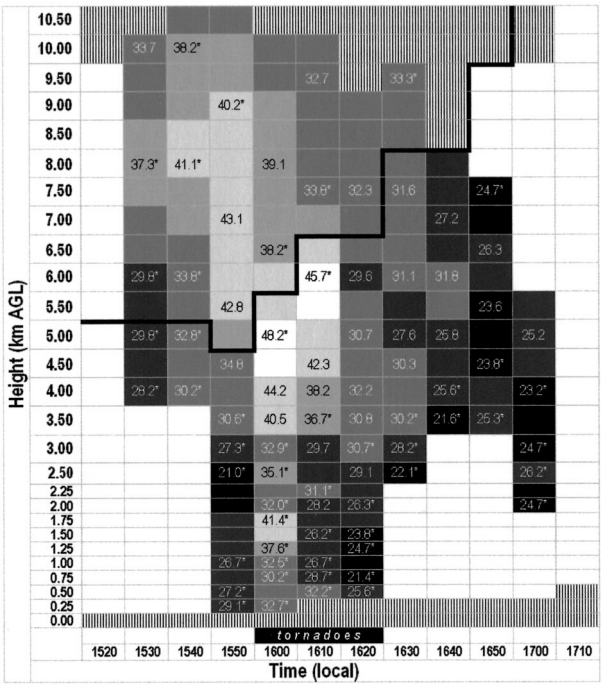


FIG. 12. Values of C-Pol maximum differential velocity (m s$^{-1}$) with time and height for areas of rotation within storm C meeting the mesocyclone identification criteria provided in section 3c. Graph shading has an interval of 5 m s$^{-1}$ and is subjectively interpolated between data points to more clearly show patterns. Values with an asterisk indicate that velocity data were missing in one or more grid squares adjacent to the grid square where the velocity maximum/minimum was located i.e., the maximum (minimum) may have been higher (lower). Times when tornadoes were occurring are shown at bottom in black. All values of MDV above the heavy black line have vertical component velocity contamination greater than 25%. Hatched areas represent heights–times where velocity data were unusable or unavailable. Heights are centered in space (i.e., 3.00 km = 2.75 to 3.20 km). Time labels indicate the beginning time (i.e., 1610 LT = 1610 to 1619 LT).

gested by the damage survey, could not have been detected explicitly in the radial velocity data since the beam diameters of both Doppler radars upon reaching the tornadoes were roughly two to three times greater than the tornado diameter (see Fig. 2). Therefore, the areas of enhanced shear likely reflect the flow of air around the tornadoes and are thus considerably weaker than what would be expected to be associated with the tornadoes themselves. Wakimoto and Wilson (1989) and Wakimoto and Liu (1998) have also documented narrow tornadoes appearing in radial velocity data as areas of weak azimuthal shear.

The positions of these shear centers between 1610 and 1630 LT were used in conjunction with photographs, eyewitness reports, and damage survey data to estimate the start and end times for the tornadoes. These times, shown in Fig. 7, are given to the nearest 5 min in recognition of the error involved. As estimated, the three tornadoes occurred between 1605 and 1625 LT, and did so simultaneously from 1610 to 1615 LT.

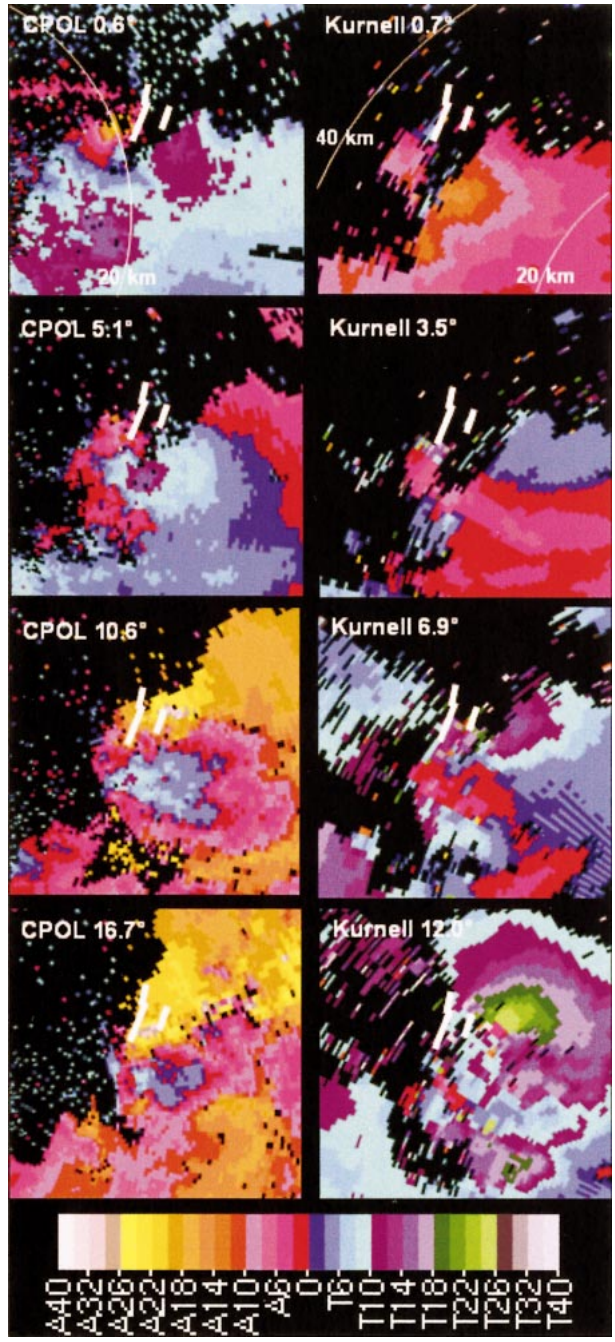


FIG. 13. CARDS images showing C-Pol (unfolded) and Kurnell radial velocities (m s$^{-1}$) at 1600 LT for 0.5, 2.0, 4.0, and 6.5 km AGL (top to bottom). Range rings with a 20-km interval are shown for the lowest-level scans. Tornado damage tracks are superimposed. Note that greater than 25% vertical component contamination is present for C-Pol 16.7°.

Though C-Pol radial velocity data support the occurrence of simultaneous tornadoes, none of the photographs is able to show this clearly.

Between 1620 and 1630 LT, MDV values at low levels fell below 20 m s$^{-1}$ and tornadic activity ceased. The

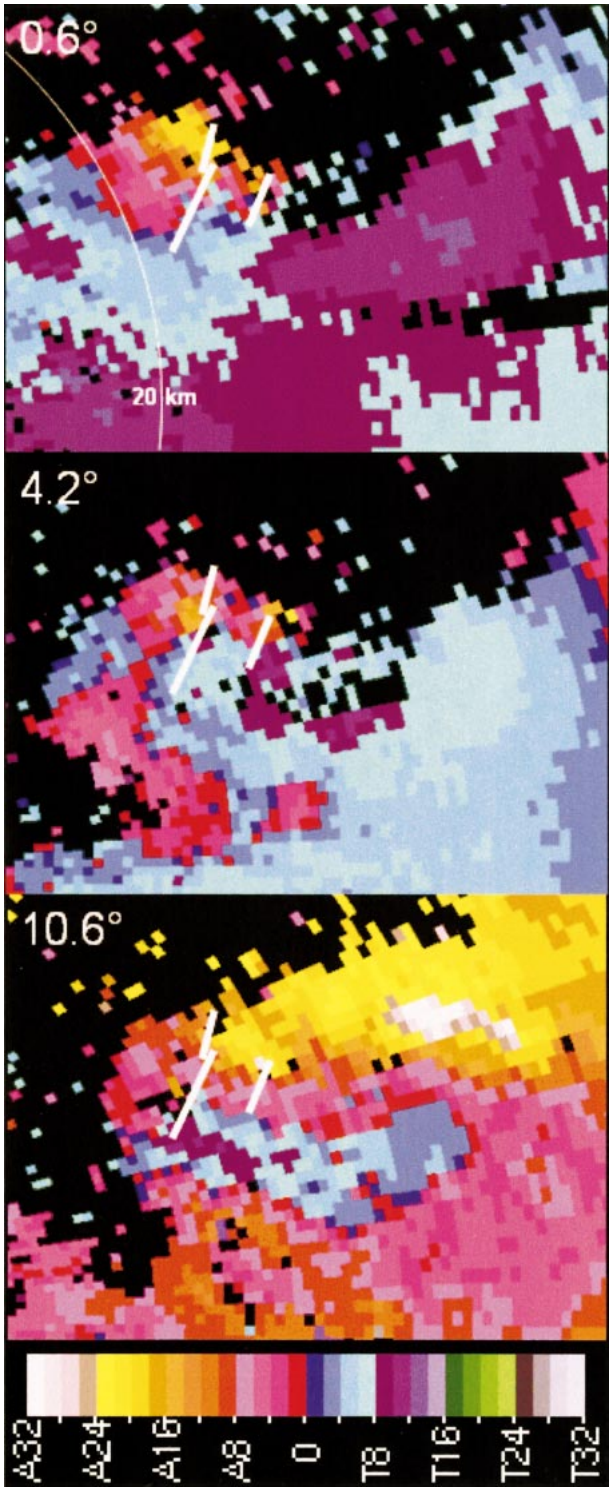


FIG. 14. CARDS images showing C-Pol (unfolded) radial velocities (m s$^{-1}$) at 1610 LT for 0.6°, 4.2°, and 10.6° scans (top to bottom). Range rings with a 20-km interval are shown for the lowest-level scan. The damage tracks for the three tornadoes are superimposed.

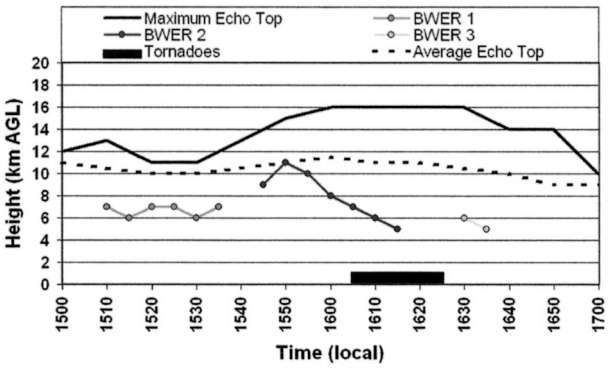


FIG. 15. Ten-minute maximum echo-top heights determined using CARDS echo-top data from the Wollongong radar and 5-min BWER heights determined with WDSS Kurnell radar data. BWER and echo-top values are those associated with storm C only. The period over which tornadoes were occurring is also labeled.

intensity of the midlevel mesocyclone also continued to decrease, as shown in Fig. 12. Between 1650 and 1700 LT, the entire midlevel mesocyclone descended as the storm rapidly collapsed. The collapse of the storm at this time can also be seen in the storm C echo-top data shown in Fig. 15, which reveals that the tornadoes developed as the most intense BWER was in the process of collapsing, a common feature of tornadic supercell storms (Lemon et al. 1978; Lemon and Doswell 1979).

## 6. Discussion

Severe storms developed in the Sydney region on 3 November under the influence of weak synoptic-scale forcing. Mesoscale factors such as differential heating, the generation of boundaries, and interactions between boundaries were clearly important from storm initiation through tornadogenesis to storm dissipation. The ability to detect and forecast such features in real time was also put to the test. As was said by Doswell et al. (1993, p. 567), ''most tornado events involve mesoscale processes that are difficult to anticipate at present.'' This statement remains true a decade later and is particularly relevant to the complex series of mesoscale events that led to the development of tornadoes on 3 November.

### *a. The role of boundaries*

The SBF and thunderstorm gust fronts were critical to the events of this day in several respects. First, the thunderstorms discussed in this study were either enhanced or initiated at boundaries. Storm A underwent rapid intensification as it encountered the SBF. Storm B was initiated when the storm A gust front interacted with the SBF. Storm C developed when a gust approaching from the northwest collided with the SBF and the storm A–B gust front. Boundaries were also responsible for initiating and/or enhancing numerous other storms on this day. However, all severe weather re-

ported in the Sydney region, including large hail, heavy rain, and tornadoes, occurred in the vicinity of *interacting* boundaries, all involving the SBF.

Second, boundaries played an important role in storm motion and lifetime. The observed average motion of storm C while possessing a midlevel mesocyclone (209° at 7.3 m $s^{-1}$) was 52° to the left of, and 2.7 m $s^{-1}$ faster than, the proximity sounding mean wind. Storm motion vectors predicted using the empirically based rule of 30° to the left, and 75% of the speed, of the mean wind (Davies and Johns 1993), and an algorithm based on the internal dynamics of supercell storms (Bunkers et al. 2000), were about 4 m $s^{-1}$ different than the observed storm motion vector (see Fig. 6).[6] The motion of storm C was similar to that of other supercells on this day when it possessed a midlevel mesocyclone and was not interacting with the triple point. Interactions with the triple point resulted in development toward the northwest and an associated change in storm motion toward the left. After 1700 LT, storm C was well separated from the triple point and its midlevel mesocyclone dissipated. Its motion quickly changed to match that of the mean wind. This suggests that storm C motion was strongly influenced by both internal supercell dynamics *and* boundary-related low-level convergence. In addition, the lifetime of storm C was enhanced by the movement of the SCGF at nearly the same speed as the storm, ensuring a continuous supply of relatively warm air and low-level convergence (Wilson and Megenhardt 1997).

Finally, boundaries were clearly important to the development of the storm C low-level mesocyclone and associated tornadogenesis. The low-level mesocyclone rapidly developed only as the triple point moved into the updraft region of the storm. The low-level mesocyclone just as quickly dissipated as the triple point moved back toward the west. Tornadoes occurred only after the low-level mesocyclone formed and they dissipated as it weakened. Storms that rapidly develop rotation at low levels after moving across and to the cool side of a boundary have also been documented by Maddox et al. (1980) and Rasmussen et al. (2000), among others.

Following Atkins et al. (1999) and Markowski et al. (1998), we think that baroclinically generated horizontal vorticity associated with air on the cool side of the sea-breeze front was tilted and stretched by the storm C updraft to form the low-level mesocyclone. The horizontal vorticity associated with air on the cool side of the SBF would have produced cyclonic rotation when tilted into the vertical.[7] The fact that the low-level mesocyclone appears in the velocity data just as the SBF approaches the updraft region appears to support this hypothesis. In addition, low-level reflectivity loops of C-Pol clear-air returns (not shown) show segments of the sea-breeze front and horizontal convective rolls rapidly accelerating toward storm C as it approached. This suggests that horizontal vorticity on the cool side of the SBF may have undergone considerable stretching even before being tilted into the storm C updraft.

The analysis of the tornado-related data suggests that each of the three observed tornadoes occurred in association with the storm C low-level mesocyclone and that the tornadoes occurred simultaneously for a short period. Though multiple simultaneous tornadoes from separate low-level mesocyclones or via nonsupercell tornadogenesis are not uncommon, the occurrence of multiple simultaneous tornadoes associated with a *single* low-level mesocyclone has rarely been documented. The tornadogenesis mechanism that appears to most closely fit observations involves cylindrical vortex-sheet instability associated with a two-celled low-level mesocyclone. This mechanism, proposed by Rotunno (1986) and recently observed by Wakimoto and Liu (1998), involves the development of a downdraft near the central axis of the mesocyclone. Vortices that are smaller in scale than the mesocyclone form at the interface between the central downdraft and the surrounding updraft. Contact with the ground results in the intensification of one or more of these vortices to tornadic strength.

If this was indeed the mechanism for tornadogenesis, one would expect to find some evidence of a downdraft at the center of the low-level mesocyclone. In fact, a divergence signature was apparent on C-Pol radar between the paths of tornadoes G and S at 1610 LT (e.g., Fig. 14, 4.2°). In addition, the damage at the Ringrose school, apparently unrelated to tornadic winds, was surveyed near this location (see Fig. 7).

### *b. Issues for operational nowcasting*

As demonstrated by the events of 3 November, boundaries such as the sea-breeze front and gust fronts can be critical to the development of severe weather. However, the state-of-the-art nowcasting systems and experts assembled for the FDP, using enhanced field observations, could produce only a limited picture of the evolution and potential importance of these boundaries in real time, and even that information was not fully utilized by the forecasters (Fox et al. 2004). Clearly, improved operational use of boundary information and a greater understanding of the relationship between boundaries and severe weather could lead to more timely and accurate severe weather warnings.

Boundary detection could be improved through changes to a variety of operational observation systems. Radar configurations could be changed to scan more frequently and at lower elevations, higher-resolution

[6] Changes to the environmental wind profile between the 1000 LT sounding time and the time of occurrence for storm C (as discussed in section 4a) may account for some of this difference.

[7] Horizontal vorticity behind the leading edge of a forward flank downdraft would also have produced cyclonic rotation when tilted. However, this boundary could not be detected with the available data and has been known to be entirely absent with some supercells (see Markowski et al. 1998).

visible satellite data could be made available at shorter time intervals, and surface observations could be more frequent as well as more dense. A mesoscale network of wind profilers could be installed. However, no one system will permit the detection of all boundaries all of the time and forecasters rarely have time to examine individual data sources thoroughly in severe weather situations.

Advanced tools are needed for real improvements in the detection of boundaries, the assessment of their potential role for severe weather, and the utility of boundary-related information in real time. We recommend a strategy for boundary analysis that involves the use of automated algorithms to identify potential boundaries using all available boundary-related data (possibly including high-resolution numerical modeling output), the visual presentation of boundary-related data and algorithm output in a simplified manner, and the use of forecaster knowledge and pattern recognition skills to confirm the existence and location of boundaries. Accurate boundary information may then be used by other algorithms to provide nowcasting guidance for such things as convective initiation and severe weather potential. ANC was the only FDP nowcasting system that used boundary information for its nowcasts, and the synthesis of a variety of data types was a key component. Subsequent changes to ANC to allow improved forecaster interaction, and the incorporation of recent work linking ANC with severe weather detection and prediction algorithm from WDSS (Roberts et al. 2001), are in keeping with the above boundary analysis strategy.

## 7. Conclusions

Data from a meteorological observational network enhanced for the Sydney 2000 Forecast Demonstration Project were analyzed to describe both the evolution of the 3 November severe thunderstorms in the western suburbs of Sydney, Australia, and the role played by low-level boundaries such as thunderstorm gust fronts and the sea-breeze front. Primary data sources included two Doppler radars, a surface mesonet, enhanced upper-air observations, storm photographs, and a damage survey. The following are the conclusions of the study.

- Though the environment in the Sydney region was conducive to the development of severe supercell thunderstorms, synoptic-scale forcing was weak. Low-level boundaries and their interactions were central to the development of the severe storms. All severe storms were initiated and/or enhanced at boundaries and all severe weather occurred in the vicinity of interacting boundaries.
- Severe weather included three tornadoes, damaging wind gusts, hail to 7-cm diameter, and heavy rain causing flash flooding. The tornadoes occurred within a 20-min period and a 3 km by 5 km area causing damage rated up to F1 on the Fujita scale.
- Nearly all of the reported severe weather was produced by one intense storm. This storm developed a midlevel mesocyclone 30 min after initiation. Its motion, well to the left of the mean flow over most of its lifetime, was strongly influenced by both internal supercell dynamics and low-level convergence related to interacting boundaries.
- This storm underwent rapid changes 50 min after initiation as a gust front forced the sea-breeze front into the storm's updraft region. A bounded weak echo region, rear-flank downdraft, low-level mesocyclone, hook echo, and rotating wall cloud rapidly developed as this occurred.
- The tornadoes developed 60–70 min after storm initiation. All three tornadoes developed from within a single low-level mesocyclone and were found to occur simultaneously for a short period. The observations suggest tornadogenesis involving cylindrical vortex-sheet instabilities within a two-celled low-level mesocyclone but confirmation was not possible with the available data.
- Both the tornadoes and the low-level mesocyclone dissipated as the sea-breeze front surged away from the updraft region, strongly suggesting that the sea-breeze front was important for their formation. It is thought that the low-level mesocyclone formed when horizontal vorticity along the cool side of the sea-breeze front was tilted and stretched by an intense updraft, as has been demonstrated in recent studies.
- Improved warning lead time and accuracy for such events requires better knowledge of the relationship between boundaries and severe weather and advanced tools to assist the forecaster with detection and nowcasting of boundaries in real time. We recommend a boundary analysis strategy that involves both automated detection algorithms and manual forecaster analysis and interaction.

*Acknowledgments.* Thanks to Patrick McCarthy, Peter Dunda, Andrew Treloar, John Bally, Alan Seed, and Clive Pierce for assistance with the damage survey and to Glen Nagle and Matthew Smith for providing photographic evidence, witness reports, and some postevent analysis. The assistance of Tom Keenan, Andrew Crook, Peter May, Cynthia Mueller, Rita Roberts, Norman Donaldson, Peter Rodriguez, Sudesh Boodoo, and Jim Young is also much appreciated. Finally, Matthew Bunkers, John Monteverdi, and two anonymous reviewers provided insightful comments that led to numerous significant improvements to the manuscript.

REFERENCES

Atkins, N. T., M. L. Weisman, and L. J. Wicker, 1999: The influence of preexisting boundaries on supercell evolution. *Mon. Wea. Rev.,* **127,** 2910–2927.

Brady, R. H., and E. J. Szoke, 1989: A case study of nonmesocyclone

tornado development in northeast Colorado: Similarities to waterspout formation. *Mon. Wea. Rev.,* **117,** 843–856.

Brooks, H. E., C. A. Doswell III, and J. Cooper, 1994: On the environments of tornadic and nontornadic mesocyclones. *Wea. Forecasting,* **9,** 606–618.

Brown, R. A., L. R. Lemon, and D. W. Burgess, 1978: Tornado detection by pulsed Doppler radar. *Mon. Wea. Rev.,* **106,** 29–38.

Bunkers, M. J., B. A. Klimowski, J. W. Zietler, R. L. Thompson, and M. L. Weisman, 2000: Predicting supercell motion using a new hodograph technique. *Wea. Forecasting,* **15,** 61–79.

BoM, 1995: Report on the 21 January 1991 Sydney severe thunderstorm. Bureau of Meteorology, Rep. F2.17, Melbourne, Australia, 26 pp.

——, 1999: Report by the Director of Meteorology on the Bureau of Meteorology's forecasting and warning performance for the Sydney hailstorm of 14 April 1999. Bureau of Meteorology, Rep. F2.20, Melbourne, Australia, 30 pp.

Corfidi, S. F., 1998: Forecasting MCS mode and motion. Preprints, *19th Conf. on Severe Local Storms,* Minneapolis, MN, Amer. Meteor. Soc., 626–629.

Crook, N. A., and J. Sun, 2001: Assimilating radar, surface and profiler data for the Sydney 2000 Forecast Demonstration Project. Preprints, *30th Int. Conf. on Radar Meteorology,* Munich, Germany, Amer. Meteor. Soc., 480–482.

Davies, J. M., and R. H. Johns, 1993: Some wind and instability parameters associated with strong and violent tornadoes 1. Wind shear and helicity. *The Tornado: Its Structure, Dynamics, Prediction, and Hazards, Geophys. Monogr.,* No. 79, Amer. Geophys. Union, 573–582.

Davies-Jones, R., and H. Brooks, 1993: Mesocyclogenesis from a theoretical perspective. *The Tornado: Its Structure, Dynamics, Prediction, and Hazards, Geophys. Monogr.,* No. 79, Amer. Geophys. Union, 105–114.

——, D. Burgess, and M. Foster, 1990: Test of helicity as a tornado forecast parameter. Preprints, *16th Conf. on Severe Local Storms,* Kananaskis Park, AB, Canada, Amer. Meteor. Soc., 588–592.

——, R. J. Trapp, and H. B. Bluestein, 2001: Tornadoes and tornadic storms. *Severe Convective Storms, Meteor. Monogr.,* No. 50, Amer. Meteor. Soc., 167–221.

Doswell, C. A., III, and E. N. Rasmussen, 1994: The effect of neglecting the virtual temperature correction on CAPE calculations. *Wea. Forecasting,* **9,** 625–629.

——, S. J. Weiss, and R. H. Johns, 1993: Tornado forecasting: A review. *The Tornado: Its Structure, Dynamics, Prediction, and Hazards, Geophys. Monogr.,* No. 79, Amer. Geophys. Union, 557–571.

Fox, N. I., and Coauthors, 2004: The impact of advanced nowcasting systems on severe weather warning during the Sydney 2000 Forecast Demonstration Project: 3 November 2000. *Wea. Forecasting,* **19,** 97–114.

Fujita, T. T., 1981: Tornadoes and downbursts in the context of generalized planetary scales. *J. Atmos. Sci.,* **38,** 1511–1534.

Geerts, B., and M. Noke-Raico, 1995: Tornadoes in Australia: Do we really know? *Bull. Austr. Meteor. Oceanogr. Soc.,* **8,** 46–51.

Joe, P., D. Burgess, R. Potts, T. Keenan, G. Stumpf, and A. Treloar, 2004: The S2K severe weather algorithms and their performance. *Wea. Forecasting,* **19,** 43–63.

Keenan, T., and Coauthors, 2002: 2000 World Weather Research Programme Forecast Demonstration Project: Overview and current status. BMRC Research Rep. 85, Bureau of Meteorology, Melbourne, Australia, 28 pp.

Lemon, L. R., and C. A. Doswell III, 1979: Severe thunderstorm evolution and mesocyclone structure as related to tornadogenesis. *Mon. Wea. Rev.,* **107,** 1184–1197.

——, D. W. Burgess, and R. A. Brown, 1978: Tornadic storm airflow and morphology derived from single-Doppler radar measurements. *Mon. Wea. Rev.,* **106,** 48–61.

Maddox, R. A., L. R. Hoxit, and C. F. Chappel, 1980: A study of tornadic thunderstorm interactions with thermal boundaries. *Mon. Wea. Rev.,* **108,** 322–336.

Markowski, P. M., E. N. Rasmussen, and J. M. Straka, 1998: The occurrence of tornadoes in supercells interacting with boundaries during VORTEX-95. *Wea. Forecasting,* **13,** 852–859.

May, P. T., 2001: Mesocyclone and microburst signature distortion with dual PRT radars. *J. Atmos. Oceanic Technol.,* **18,** 1229–1233.

Mitchell, E., and D. Griffiths, 1993: Report on the Sydney Hailstorm, March 1990. Phenomena Rep. F2.16, Bureau of Meteorology, Melbourne, Australia, 44 pp.

Moller, A. R., C. A. Doswell III, M. P. Foster, and G. R. Woodall, 1994: The operational recognition of supercell thunderstorm environments and storm structures. *Wea. Forecasting,* **9,** 327–347.

Monteverdi, J. P., W. Blier, G. Stumpf, W. Pi, and K. Anderson, 2001: First WSR-88D documentation of an anticyclonic supercell with anticyclonic tornadoes: The Sunnyvale–Los Altos, California, tornadoes of 4 May 1998. *Mon. Wea. Rev.,* **129,** 2805–2814.

Potts, R. J., T. D. Keenan, and P. T. May, 2000: Radar characteristics of storms in the Sydney area. *Mon. Wea. Rev.,* **128,** 3308–3319.

Purdom, J. F. W., 1976: Some uses of high-resolution GOES imagery in the mesoscale forecasting of convection and its behavior. *Mon. Wea. Rev.,* **104,** 1474–1483.

Rasmussen, E. N., J. M. Straka, R. Davies-Jones, C. A. Doswell III, F. H. Carr, M. D. Eilts, and D. R. MacGorman, 1994: Verification of the Origins of Rotation in Tornadoes Experiment: VORTEX. *Bull. Amer. Meteor. Soc.,* **75,** 995–1006.

——, S. Richardson, J. M. Straka, P. M. Markowski, and D. O. Blanchard, 2000: The association of significant tornadoes with a baroclinic boundary on 2 June 1995. *Mon. Wea. Rev.,* **128,** 174–191.

Roberts, R. D., D. Burgess, and M. Meister, 2001: Next steps in automated thunderstorm nowcasting: Improving performance and forecasting storm severity. Preprints, *30th Int. Conf. on Radar Meteorology,* Munich, Germany, Amer. Meteor. Soc., 234–236.

Rotunno, R., 1986: Tornadoes and tornadogenesis. *Mesoscale Meteorology and Forecasting,* P. S. Ray, Ed., Amer. Meteor. Soc., 414–436.

——, and J. B. Klemp, 1985: On the rotation and propagation of simulated supercell thunderstorms. *J. Atmos. Sci.,* **42,** 271–292.

Sills, D., P. Taylor, P. King, W. Hocking, and I. Nichols, 2002: ELBOW 2001—Studying the relationship between lake breezes and severe weather: Project overview and preliminary results. Preprints, *21st Conf. on Severe Local Storms,* San Antonio, TX, Amer. Meteor. Soc., 611–614.

Trapp, R. J., and R. Davies-Jones, 1997: Tornadogenesis with and without the dynamic pipe effect. *J. Atmos. Sci.,* **54,** 113–133.

Wakimoto, R. M., and J. W. Wilson, 1989: Non-supercell tornadoes. *Mon. Wea. Rev.,* **117,** 1113–1140.

——, and C. Liu, 1998: The Garden City, Kansas, storm during VORTEX 95. Part II: The wall cloud and tornado. *Mon. Wea. Rev.,* **126,** 393–408.

——, ——, and H. Cai, 1998: The Garden City, Kansas, storm during VORTEX 95. Part I: Overview of the storm's life cycle and mesocyclogenesis. *Mon. Wea. Rev.,* **126,** 372–392.

Weaver, J. F., 1979: Storm motion as related to boundary-layer convergence. *Mon. Wea. Rev.,* **107,** 612–619.

Weckwerth, T. M. and D. B. Parsons, 2002: An overview of the International $H_2O$ Project (IHOP_2002). Preprints, *21st Conf. on Severe Local Storms,* San Antonio, TX, Amer. Meteor. Soc., 279–282.

Weisman, M. L., and J. B. Klemp, 1984: The structure and classification of numerically simulated convective storms in directionally varying wind shears. *Mon. Wea. Rev.,* **112,** 2479–2498.

——, and ——, 1986: Characteristics of isolated convective storms. *Mesoscale Meteorology and Forecasting,* P. S. Ray, Ed., Amer. Meteor. Soc., 331–358.

——, and R. Rotunno, 2000: The use of vertical wind shear versus helicity in interpreting supercell dynamics. *J. Atmos. Sci.,* **57,** 1452–1472.

Weiss, C. C., and H. B. Bluestein, 2002: Airborne pseudo-dual-Doppler analysis of a dryline–outflow boundary intersection. *Mon. Wea. Rev.,* **130,** 1207–1226.

Wicker, L. J., and R. B. Wilhelmson, 1995: Simulation and analysis of tornado development and decay within a three-dimensional supercell thunderstorm. *J. Atmos. Sci.,* **52,** 2675–2703.

Wilson, J. W., and W. E. Schreiber, 1986: Initiation of convective storms at radar-observed boundary-layer convergence lines. *Mon. Wea. Rev.,* **114,** 2516–2536.

——, and D. L. Megenhardt, 1997: Thunderstorm initiation, organization, and lifetime associated with Florida boundary layer convergence lines. *Mon. Wea. Rev.,* **125,** 1507–1525.

——, E. E. Ebert, T. R. Saxen, R. D. Roberts, C. K. Mueller, M. Sleigh, C. E. Pierce, and A. Seed, 2004: Sydney 2000 Forecast Demonstration Project: Convective storm nowcasting. *Wea. Forecasting,* **19,** 131–150.

Ziegler, C. L., E. N. Rasmussen, T. R. Shepherd, A. I. Watson, and J. M. Straka, 2001: The evolution of low-level rotation in the 29 May 1994 Newcastle–Graham, Texas, storm complex during VORTEX. *Mon. Wea. Rev.,* **129,** 1339–1368.